Energy materials

Co$_3$O$_4$-C yolk-shell hollow spheres derived from ZIF-12-PVP@GO for superior anode performance in lithium-ion batteries

Xingxing Ding[1], Xianghong Ge[1,*], Congcong Xing[2], Yanyan Liu[3,4], Tongjun Li[2], Xingsheng Li[2], Tianlei Ma[2], Ruofan Shen[2], Erjun Liang[2], Huaqiang Cao[5], and Baojun Li[1,*] (iD)

[1] *Zhengzhou Key Laboratory of Low-Dimensional Quantum Materials and Devices, College of Science, Zhongyuan University of Technology, 41 Zhongyuan Road, Zhengzhou 450007, People's Republic of China*

[2] *Research Center of Green Catalysis, College of Chemistry, School of Electrical Engineering, Zhengzhou University, 100 Science Road, Zhengzhou 450001, People's Republic of China*

[3] *College of Science, Henan Agricultural University, 95 Wenhua Road, Zhengzhou 450002, People's Republic of China*

[4] *Institute of Chemical Industry of Forest Products, National Engineering Labortatory for Biomass Chemical Utilization, Nanjing 210042, People's Republic of China*

[5] *Department of Chemistry, Tsinghua University, Beijing 100084, People's Republic of China*

ABSTRACT

Transitional metal oxides have attracted increasing attention as the most promising anode material for lithium-ion batteries (LIBs). However, due to the poor ionic conductivity and great structural changes in the process of Li$^+$ insertion and extraction, the performance of the pristine materials in batteries still has a far way to go to satisfy requirements. In this article, using spherical ZIF-12 as a pyrolysis precursor, two Co$_3$O$_4$ hollow core-shell carbon nanocomposites (CHS@C and CHS@CG) were fabricated via a molecular precursor pyrolysis strategy. The synergistic effect of the yolk-shell hollow nanosphere structure shortens the diffusion path of ions, increases the contact area between the electrode and electrolyte, and provides a buffer space for the volume change in the electrochemical reaction. Both materials have excellent structural stability and good electrical conductivity. In comparison, the performance of CHS@CG is better, and the reversible specific capacity reaches 831 mAh·g^{-1} at 0.2 C after 400 cycles. In the galvanostatic charge–discharge process, the Coulombic efficiency reaches nearly 100%, exhibiting a good reversible cycle. The synthesis method of these electrode materials can provide a reference for making other energy storage equipments.

🖄 Springer

GRAPHICAL ABSTRACT
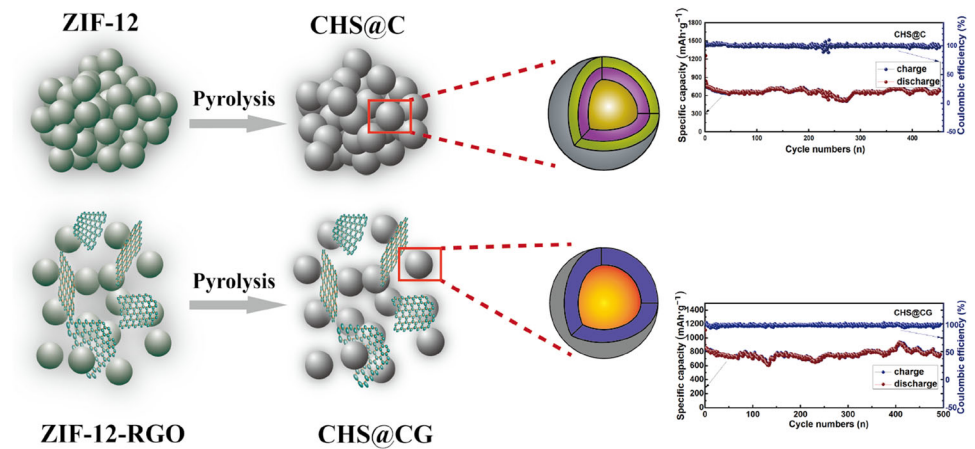
Introduction

With the rapid development of the world economy and the shortage of nonrenewable resources such as fossil fuels, finding alternative green energy has become an urgent research topic for researchers [1]. Lithium-ion batteries (LIBs) have attracted extensive attention and in-depth research in light of their advantages of high energy density, large output power, cycle stability, no memory effect, long lifespan, and environmental friendliness [2]. Today, LIBs have become the dominant power source in our lives, from small portable electronic devices to large electric and hybrid electric vehicles [3, 4]. However, graphite, as a widely used anode material, has ideal cycling performance, and its low theoretical specific capacity seriously affects the performance of LIBs [5]. Based on this, researchers have constantly looked for excellent anode materials in recent years. Transition metal oxides (TMOs) as electrode materials have attracted significant attention for their rich resources and high capacity [6–8]. For example Fe_2O_3 [9], Fe_3O_4 [10], NiO [11], CuO [12], MnO_2 [13], and various TMOs (M = Ni, Co, Cu, Ti, etc.) [14, 15] have been intensively studied in LIBs. Among these metal oxides, Co_3O_4 nanomaterials are the most prominent anode materials for LIBs in light of their high theoretical specific capacities, diversity of oxidation valence, and environmental friendliness. Co_3O_4 can

be obtained from natural abundant and inexpensive resources [16, 17]. However, there are also some severe drawbacks that are similar to those of other pristine TMOs, such as perishing cycle stability and poor ionic conductivity.

To overcome the unilateral problem of materials, combining the advantages of different materials, using a carbon layer to wrap cobalt tetroxide is a breakthrough attempt [18]. Hollow structured micro-/nanospheres, due to their unique electrochemical properties, such as low density, large specific surface area, good thermal stability, strong surface permeability, and relatively large internal space, are attracting increasing research [19–24]. Specifically, yolk-shell nanostructure materials as a special structure of LIB anode materials have received robust attention. In contrast to the general core-shell structure, the yolk-shell nanostructure materials with a movable space inside the protecting shell can effectively adjust the spatial variation compared to hollow nanostructures [25]. As a promising precursor at present, metallic organic frameworks (MOFs) have highly ordered permanent pore structures [26] and have been commonly prepared for hollow structures after thermal decomposition [27, 28]. Through high-temperature pyrolysis, abundant organic ligands in MOFs become well-suited carbon sources for the synthesis of porous carbon and metal-doped carbon [29]. With this consideration

in mind, Co_3O_4 yolk-shell hollow spheres covered by carbon are considered to be suitable for use in the upgrade of LIBs. For example, Chen and coworkers synthesized Co_3O_4 hollow nanofiber through template-based engineering, and Lou and coworkers designed a multistep approach to prepare hierarchical tubular structures, both of which showed somewhat improved reversible specific capacity [30–32]. Some MOFs, such as MOF-5, MOF-74, ZIF-8, ZIF-11, ZIF-67, and ZIF-68, have been used as templates for fabricating nanoporous carbons [26, 33, 34]. Through calcining MOF precursors in controlled atmospheres, Mai and coworkers designed hierarchical yolk-shell Co_3O_4/C dodecahedrons which showed excellent cycling stability [30, 35]. However, the above materials reported are more single-shell structures obtained through complicated synthesis approaches. Hollow multishell structures (HoMSs) are defined as those built up with at least two shells and two corresponding internal voids. Unlike single-shell materials, they are suggested intensively as electrodes [19, 36–42]. Higher volume energy density and better structural stability have helped them to become potential electrodes in energy storage applications [43–45]. Recently, Altin S, Yaşar S, and coworkers using ZIF-12 as the precursor synthesized unique transition metal-doped carbon composite materials, improving the electrochemical performance of the lithium-ion batteries [26, 46]. However, to date, accurately and effectively designing multishell hollow sphere structures is still a challenge.

Compared with ball milling [47], hydrothermal [48], and solvothermal methods [49], the molecular precursor pyrolysis strategy can accurately regulate the crystal phase, composition, and morphology of the target product by changing the experimental parameters [50]. In this paper, with spherical ZIF-12 as a molecular precursor for pyrolysis, two carbon materials CHS@C and CHS@CG were obtained. The preparation method is simple, universal, and repeatable. Because of the excellent electrical conductivity of graphene and the interfacial synergistic effect between Co_3O_4 and rGO, the prepared hollow nanostructure microspheres CHS-400 show excellent Li-storage capacity. The specific capacities reach 645 and 831 mAh·g^{-1}, respectively, after 400 cycles at the rate of 0.2 C, and in the constant charging and discharging process, the Coulombic efficiency reaches nearly 100%, exhibiting a good reversible cycle. Both materials have excellent structural stability and

excellent conductivity. By comparison, CHS@CG has better cyclic stability in LIBs due to the unique yolk-shell architecture filled with and covered by graphene sheets. The above effective design ideas for synthetic methods will be conducive to the development of electrodes for LIBs and the preparation of other TMOs of electrode materials and other energy storage devices.

Results and discussion

Scheme 1 illustrates the detailed formation process of CHS@C and CHS@CG. Carbon-wrapped Co_3O_4 hollow sphere structures (CHS@C and CHS@CG) are obtained after ZIF-12-1.0 g PVP calcination at 400 °C in an air atmosphere. Due to the addition of PVP, ZIFs have changed from a previously angular structure into a spherical framework compound with metal Co^{2+} as the center and ligand assembly (Fig. S1, Fig. S2). Due to the excellent thermal conductivity of graphene, the rapid heat transfer in the pyrolysis process leads to the formation of a double-layer Co_3O_4 yolk-shell hollow sphere structure (CHS@CG) with the addition of graphene. Without the addition of graphene, a multilayer Co_3O_4 hollow sphere structure (CHS@C) will form due to the gradual heat transfer process. Carbon in the structure of both materials comes from the pyrolysis of the ligand benzimidazole, and the CHS@CG material is also filled with and covered by graphene sheets from the pyrolysis of graphene. Both materials have excellent structural stability and excellent conductivity. In comparison, CHS@CG has better cyclic stability in LIBs due to the role of graphene.

The microstructure of Co-MOFs is observed by TEM images. ZIF-12-XX g-PVP possesses a different morphology and structure with different amounts of PVP. ZIF-12 does not clearly change at 0.5 g of PVP (Fig. S3), the weight of PVP increases to 1 g, and the shape is changed and becomes sphere-like (Fig. S2). This phenomenon is not an accident; even if the amount of PVP is increased to 1.5 g, the shape is still sphere-like (Fig. S4), so we selected 1 g PVP conditions to perform more individual studies.

The yolk-shell-structured hollow carbon spheres (CHS@C and CHS@CG) are obtained after calcination at 400 °C in an air atmosphere. They have a well-retained sphere-like structure even after heating. ZIF-12-PVP (1.0 g) is exposed to air at 400 °C to obtain

Scheme 1 Synthesis route and structure of CHS@C and CHS@CG.
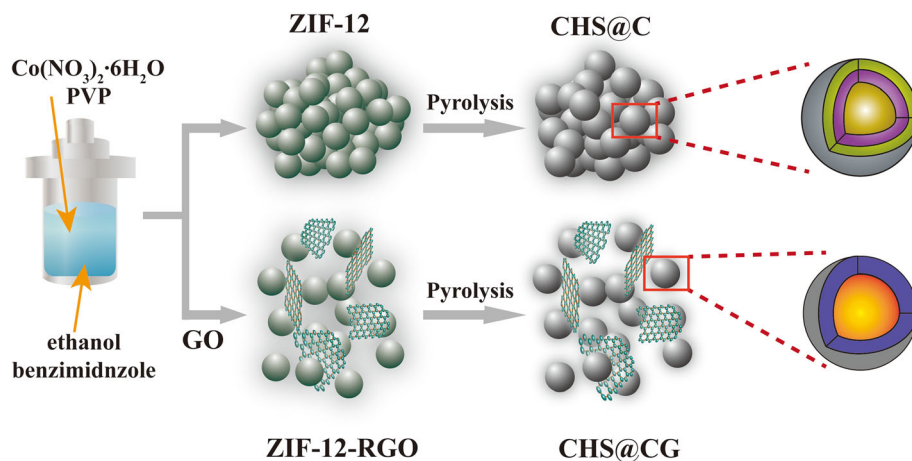
Co_3O_4 yolk-shell hollow nanospheres with multilayer structure CHS@C, and ZIF-12-PVP (1.0 g) with graphene is heated to form double-layer yolk-shell hollow nanospheres CHS@CG. The edge of CHS@CG (Fig. 1a–d) is less lucid than CHS@C (Fig. 1e–h) after 400 °C. The reason for the formation of the edge structure is that the graphene parcels ZIF-12-1.0 g-PVP and turns into carbon wrapped in the surface of the hollow spheres after pyrolysis. Therefore, there are layers of carbon around the edges (lattice spacing d = 0.33 nm). After pyrolysis of ZIFs in air, Co_3O_4 is mainly formed (lattice spacing d = 0.28 nm) [51], which is consistent with the expectation. The microstructures of ZIF-12 and ZIF-12-GO without PVP are shown in Fig. S5. Cobalt oxide exists as

Co_3O_4 above 400 °C, and the polyhedron of Co_3O_4 nanoparticles grows on GO in ZIF-12-GO-400.

The phase purity and composition of the samples were checked with X-ray diffraction (XRD). Figure S6a-c shows the XRD pattern of ZIF series materials. The phase structures of ZIF-12, ZIF-12 with 0.5 g, 1.0 g, 1.5 g, 2.0 g PVP and ZIF-12-GO with 0.5 g, 1.0 g, 1.5 g, 2.0 g PVP have little discernible difference. Therefore, the ZIFs could be defined as the ZIF-12-XX series (JCPDS No.80–0382) [52]. By comparing Fig. S6b with S6a, it can be seen that there is a broad peak at approximately 20° for ZIF-12-GO, ZIF-12-0.5 g PVP-GO, ZIF-12-1.5 g PVP-GO, and ZIF-12-2.0 g PVP-GO, which indicates the existence of graphene. The diffraction peaks at 19.0°, 31.5°, 36.8°, 38.7°, 44.8°, 55.6°, 59.4°, and 65.3° corresponding to
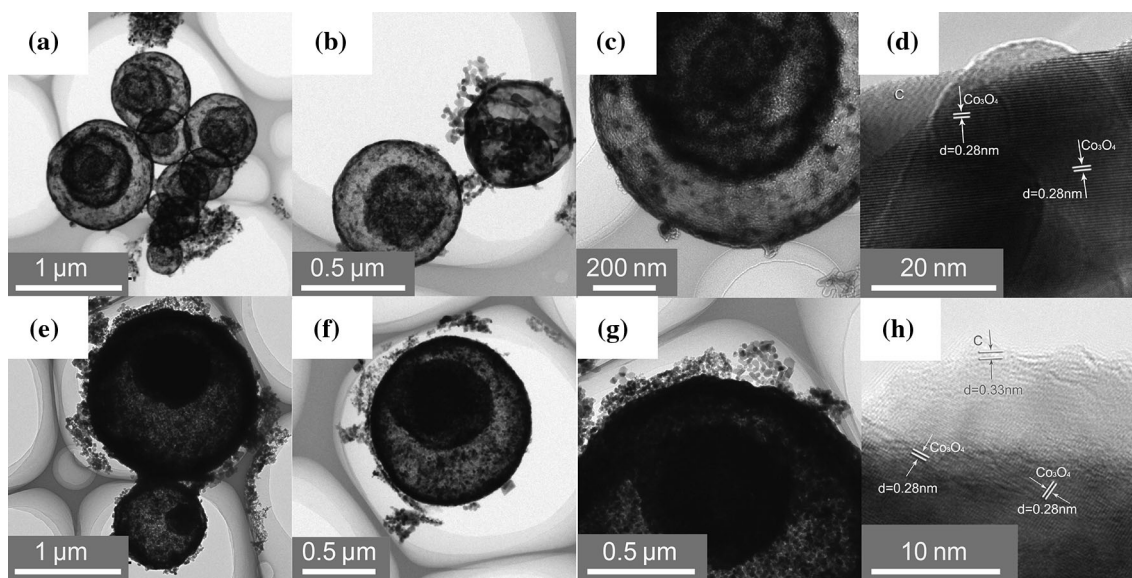

**Figure 1** TEM images of **a**–**d** CHS@C and **e**–**h** CHS@CG.

the (111), (220), (311), (222), (400), (422), (511), and (440) lattice planes are characteristic diffraction peaks of Co_3O_4 (Fig. 2a) (JCPDS No. 42–1467). This shows that the CHS@C and CHS@CG composites are obtained by annealing the ZIF-12 composites at 400 °C in air. The existing form of Co is Co_3O_4, which is completely consistent with the peak of pure $Co(NO_3)_2\cdot6H_2O$ at 400 °C in air, so it could be indicated that the existing metal oxides are Co_3O_4. ZIF-12-400 and ZIF-12-GO-400 (without PVP) have the same effect (Fig. S6d).

Figure 2b is the Raman spectra of CHS@C and CHS@CG. The diffraction peaks approximately 191, 466, 509, 600, and 670 cm^{-1} are revealed in CHS@C and CHS@CG. These are characteristic peaks of Co_3O_4, in accordance with the five Raman active modes (F_{2g}, E_g, F_{2g}, F_{2g}, A_{1g}) of the spinel Co_3O_4 phase [53]. It is further proven that the synthesized material is pure Co_3O_4 without any impurities. From the graph, we can see that the position of the A_{1g} peak in Co_3O_4 (670 cm^{-1}) is slightly lower than that of CHS@C and CHS@CG (680 cm^{-1}) because of the trace N-doped carbon coating on the nanocomposites [19]. All of these results are consistent with the XRD results.

To obtain an appropriate calcination temperature from converting the precursor into Co_3O_4, TGA–DSC was carried out on the precursors (ZIF-12-PVP and

Figure 2 a XRD patterns of CHS@C and CHS@CG; b Raman spectra of CHS@C and CHS@CG; TG curves of c ZIF-12-PVP, ZIF-12-PVP-GO and d CHS@C, CHS@CG; N_2 adsorption–desorption isotherms of e CHS@C and f CHS@CG at 77 K.
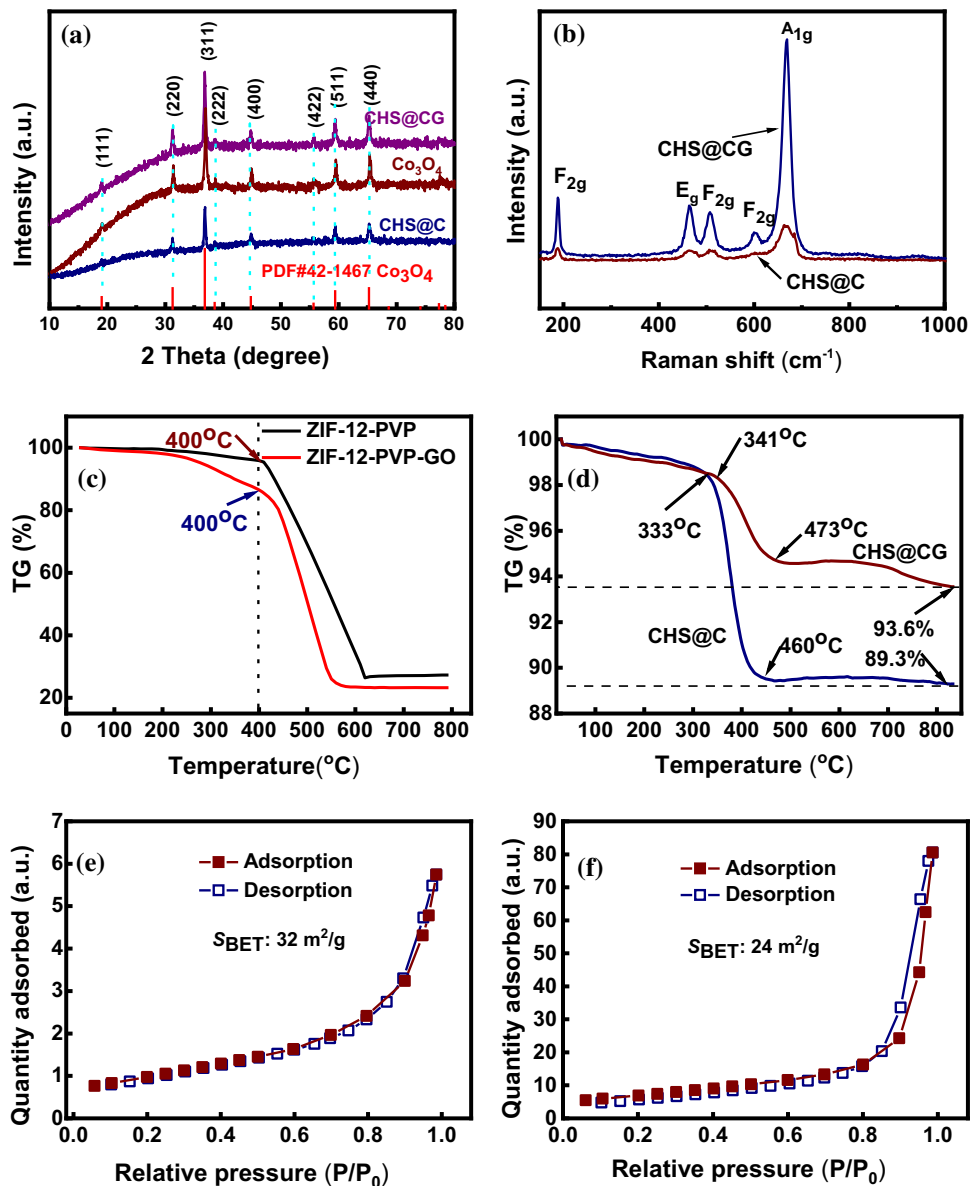
ZIF-12-PVP-GO), as shown in Fig. 2c, in an air atmosphere. From the curves, we can see there is a slight mass change from 40 °C because of the sublimation of the residual moisture in the composites. A small mass loss appears after 200 °C, which may derive from the decomposition of a few ligands. From 400 °C, there is a significant mass loss due to the pyrolytic decomposition of ligands and the oxidation of Co(NO₃)₂ to Co₃O₄ [54]. From 600 °C, there is a plateau of the mass equilibrium where the main component is Co₃O₄. Therefore, 400 °C is selected as the temperature of pyrolysis in air [36]. Figure 2d shows the TG curves of CHS@C and CHS@CG. From the TG curves, it can be seen that 0.1% of the sample mass lost occurred between 100 and 200 °C. The loss of TG quality may be due to the moisture in the sample sublimation remaining. From 330 and 340 °C to 460 and 470 °C, the obvious mass loss is attributed to the decomposition of carbon shells and graphene in the composites. By calculation, the content of Co₃O₄ in CHS@C is 89.3 $wt\%$, and in CHS@CG, it is 93.6 $wt\%$ [55].

The specific surface area and pore structure of CHS@C and CHS@CG were obtained from the N_2 adsorption–desorption isotherms measured at 77 K (Fig. 2e, f). From the adsorption branch of the isotherm curve, the specific surface area was calculated using the BET method. The BET specific surface areas are 32 and 24 $m^2 \cdot g^{-1}$ for CHS@C and CHS@CG, respectively [56]. The S_{BET} of CHS@CG is slightly smaller than that of CHS@C, which can be explained by the fact that the specific surface area of graphene shells in CHS@CG is lower than that of amorphous carbon in CHS@C after pyrolysis. This result is perfectly consistent with the electron microscopy. An appropriate specific surface area will have a positive effect on the performance in LIBs, because the moderate specific surface area in LIBs is conducive to the insertion and extraction of lithium ions [57].

To further determine the valences and the chemical composition of CHS@C and CHS@CG hollow nanospheres, X-ray photoelectron spectroscopy (XPS) measurements were taken (Fig. 3). As shown in Fig. 3e, f, the XPS full survey scan spectra confirm the presence of C, N, Co, and O atoms in the CHS@C and CHS@CG samples. The high-resolution spectra of C1s and O1s are shown in Fig. 3a–d. In the C1s spectra, the peaks at 284.4 eV, 285.1 eV, and 288.7 eV correspond to C − C, C − O, and C = O groups, respectively. In the O1s spectra, from the peaks of

Co = O (529.7 eV), Co − O (530.0 eV), and O = C (532.7 eV), it can be concluded that carbon exists in the pyrolysis process of the ZIF series, and the existing carbon is inserted into the middle of Co₃O₄ to form the carbon-doped Co₃O₄ nanohollow sphere structure, which contributes to the conductivity of the composite nanohollow sphere and improves its electrochemical performance. From the N1s spectra of the CHS@C and CHS@CG in Fig.S7a and S7c, the characteristic peaks of N1s can be attributed to the pyrrolic-N and trace graphitic-N [46]. Figure S7b and S7d shows the Co2p spectra of CHS@C and CHS@CG, in which the peaks at 797.1 eV and 782.3 eV correspond to the presence of Co2p$_{1/2}$ and Co2p$_{3/2}$, respectively, proving that cobalt exists in the form of the Co₃O₄ state, which is consistent with reports in the literature [58, 59].
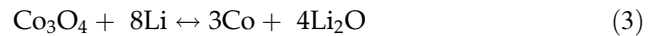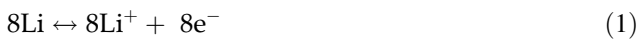
Figure 4a, b presents cyclic voltammetry (CV) curves of CHS@C and CHS@CG in the voltage range of 0.01–3.0 V at a scanning rate of 0.1 mV·s^{-1} for the initial three cycles. As shown in the figure, the two potentials of 0.85 V and 2.08 V correspond to the cathodic peak and anodic peak of Li$^+$ in the Co₃O₄-C material during insertion and extraction, respectively, namely, the reduction peak and oxidation peak. Figure 4a shows that the current intensity of the CHS@C composite decreases significantly in the first three cycles, and the first current is significantly stronger than the second and third cycles, while the current intensity of the CHS@CG (Fig. 4b) composite is more stable than that of CHS@C, and the difference between the first current intensity and the second and third cycles is not significant, suggesting good reversibility and stability [60]. This phenomenon shows that the carbon-wrapped form of CHS@CG has better stability than the carbon-free CHS@C, and the outer layer carbon shell provides protection for its volume change in the charging and discharging process [61].

Figure 4c, d shows the galvanostatic charge–discharge curves of CHS@C and CHS@CG in the voltage range of 0.01–3.0 V versus Li/Li$^+$ at the rate of 0.2 C. As seen from Fig. 4d, the CHS@CG discharge specific capacity of the first cycle (1110 mAh·g^{-1}) is higher than the theoretical value and the second cycle (846 mAh·g^{-1}). The initial capacity loss can be ascribed to the decomposition of the electrolyte and the formation of a solid electrolyte interface (SEI) membrane [62]. As shown in the figure, the voltage curve exhibits a good charge–discharge platform in 1–4 cycles

Figure 3 XPS spectra of **a**, **c** C1s, **b**, **d** O1s in CHS@C and CHS@CG, and **e**, **f** full survey of CHS@C and CHS@CG.
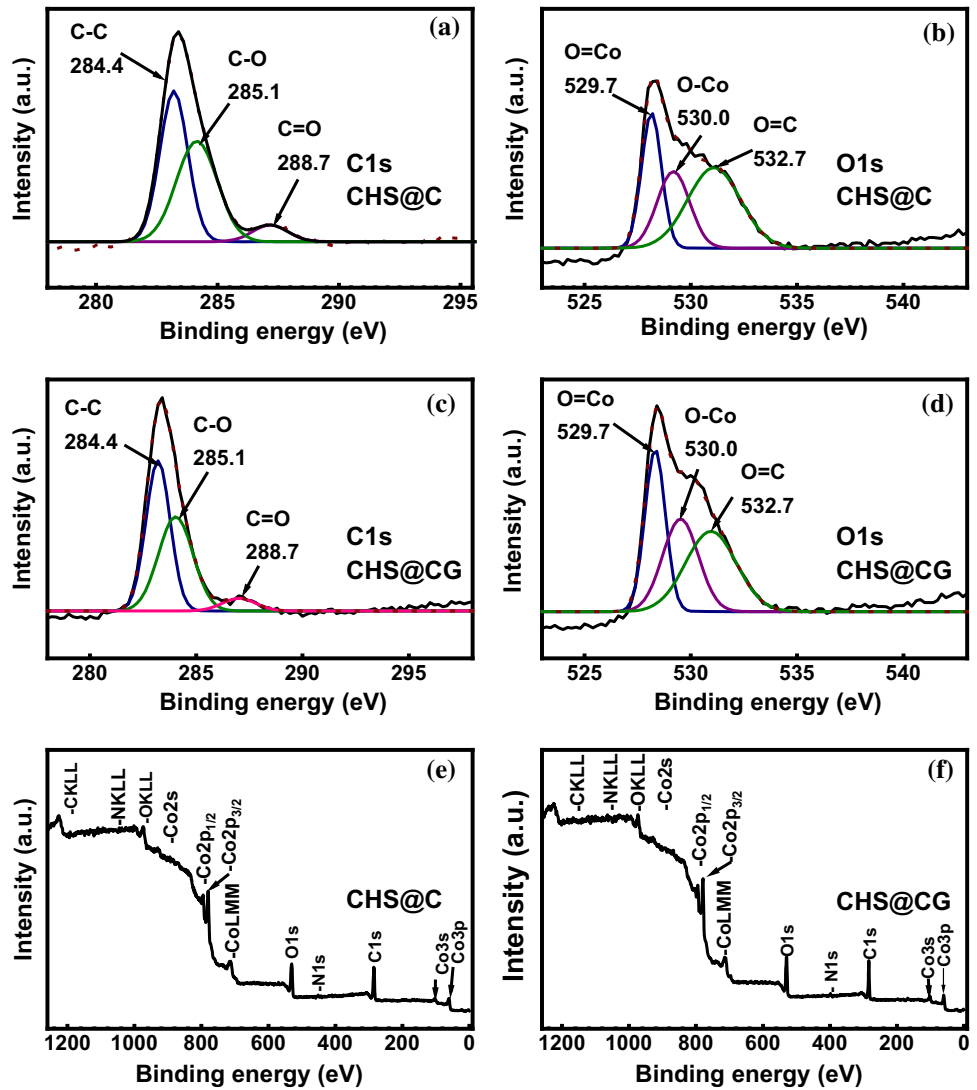

and displays good cycling stability. In Fig. 4c, the CHS@C discharge specific capacity of the first cycle (1256 mAh·g^{-1}) is higher than the theoretical value and the second cycle (835 mAh·g^{-1}), and the voltage curve has a good charge–discharge platform. Due to the hollow spherical structure, the two samples have the desired reversibility, because the electrolyte can penetrate into the hollow cavity, making the insertion and extraction of lithium ions more rapid [63]. From the figure we can see that CHS@CG has a much better reversibility. Combined with the above analysis, the CHS@C and CHS@CG lithium storage mechanisms can be illustrated by the following equations:

$$8Li \leftrightarrow 8Li^+ + 8e^- \tag{1}$$

$$Co_3O_4 + 8Li^+ + 8e^- \leftrightarrow 3Co + 4Li_2O \tag{2}$$

$$Co_3O_4 + 8Li \leftrightarrow 3Co + 4Li_2O \tag{3}$$

Multiplier performance is one of the important parameters to evaluate the performance of lithium-ion batteries. Figure 5a,b shows the rate performance of the two electrode materials at various rates with 10 charging and discharging tests. As demonstrated in the graphs, the discharge specific capacity is attenuated as the current density increases. The specific capacity decays significantly when the current density rises to 1 C and 2 C. This can be attributed to two reasons: one is the insufficient diffusion coefficient of lithium ions, and the other is volume change in the process of lithium-ion insertion and extraction under

Figure 4 CV curves of **a** CHS@C and **b** CHS@CG at 0.1 mV·s^{-1} for the initial three cycles; charge/discharge voltage profiles of **c** CHS@C and **d** CHS@CG samples at the rate of 0.2 C with four cycles.
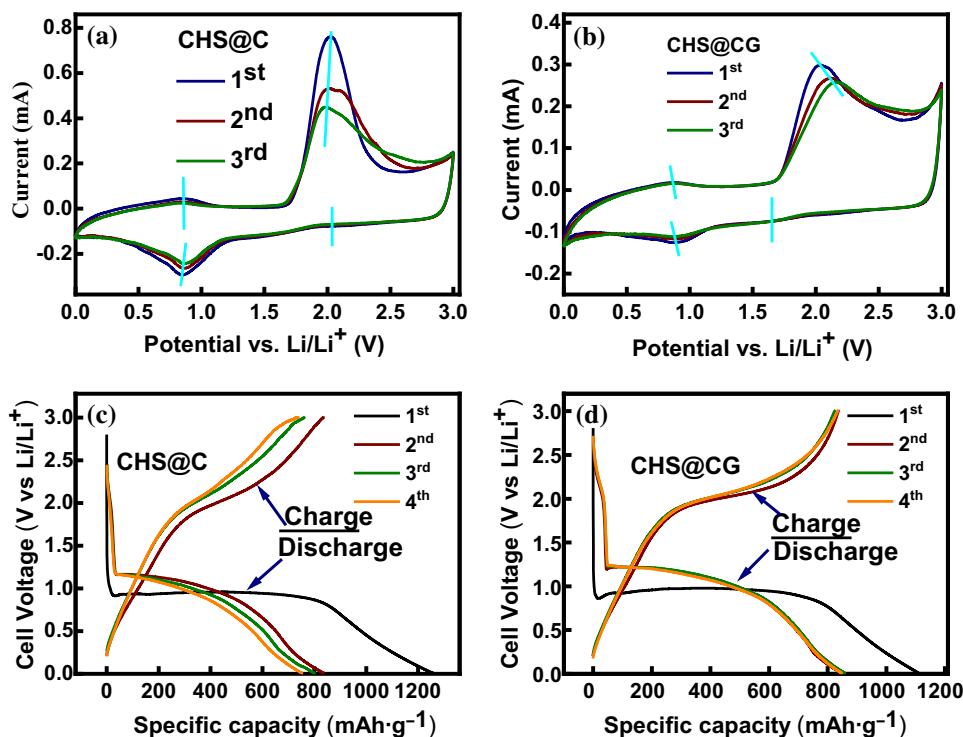

a high current density [64]. As the rate returns to the initial 0.2 C, the specific capacity is recovered to the original specific capacities. This indicates that the hollow sphere structures can tolerate changes of such high rates, show robust rate performance, and demonstrate good reaction kinetics of Co$_3$O$_4$ hollow sphere structures [65]. Compared with Fig. 5a and 5b, CHS@CG has outstanding performance. The possible reason is that the double-layer yolk-shell hollow nanosphere CHS@CG enables the insertion and extraction of lithium ions to be faster, and the good thermal conductivity of graphene makes CHS@CG have better crystallinity than CHS@C, which improves the stability of CHS@CG.

As seen from the constant current charge–discharge diagram at the rate of 0.2 C (Fig. 5c, d), the reversible specific capacity is almost unchanged as the number of cycles increases, and the battery still has a high charge–discharge capacity even after 500 cycles, showing the excellent cycle stability of lithium-ion batteries. After 400 cycles, the discharge specific capacities of CHS@C and CHS@CG are 645 mAh·g^{-1} and 831 mAh·g^{-1}, respectively, which are 74% and 95% of the theoretical value (872 mAh·g^{-1}). Relative to CHS@C composites, CHS@CG carbon shows better stability, because most of the outer layer of carbon from carbonated graphene provides a

volume change buffer space in the process of lithium-ion transport, making its structure without being destroyed, and the carbon in the outermost layer can also constrain the volume change [66]. The Coulombic efficiencies of the two electrodes are stable and nearly 100%. The sample in this research shows decent lithium storage performance compared with the other Co-bases and Co$_3$O$_4$ anode materials (Table 1).

Figure 5e–g shows the electrochemical impedance spectra (EIS) of CHS@C and CHS@CG during various charge and discharge processes. The curve consists of a semicircle in the high-middle frequency range and a slant line in the low-frequency range. The slant line represents the diffusion degree of lithium ions. The larger the slope of the slant line is, the faster the diffusion of lithium ions and the better the electrochemical properties of the material. The semicircular arc represents the resistance of charge transfer in the middle- and high-frequency regions. The higher the activity of the electrode material is, the smaller the diameter of the semicircular arc. As shown in the picture, without the electrode reaction, the migration resistance of CHS@CG is only 43 Ω, and the transfer resistances are 90 Ω and 145 Ω after 100 cycles and 500 cycles, respectively. Correspondingly, the migration resistance of CHS@C is 56 Ω without the

Figure 5 Cycling performance at various rates and corresponding Coulombic efficiency profiles of **a** CHS@C and **b** CHS@CG; cycling performance at the rate of 0.2 C and corresponding Coulombic efficiency profiles of **c** CHS@C and **d** CHS@CG; EIS spectra of CHS@CG and CHS@C **e–g** after 0, 100, and 500 cycles.
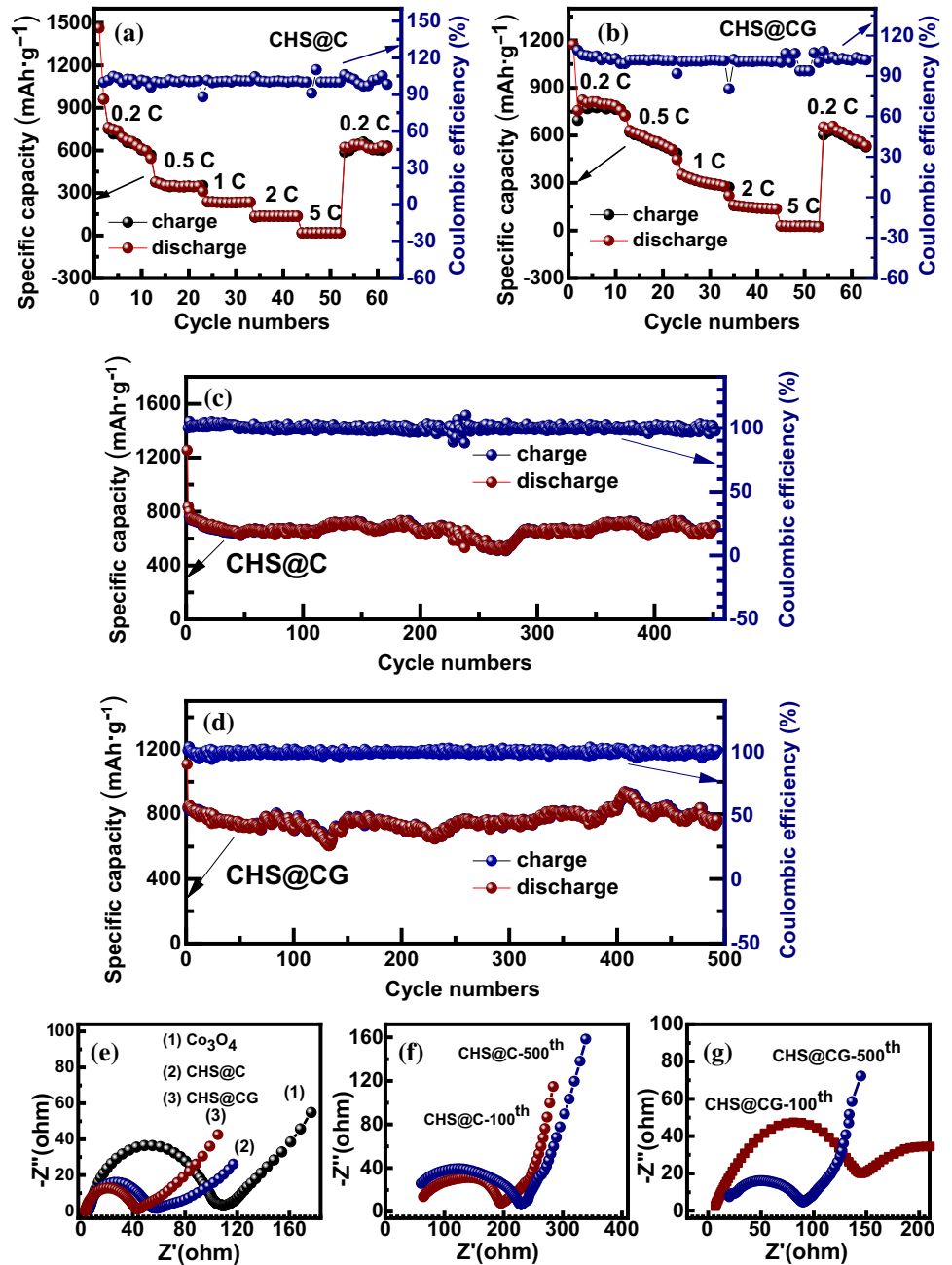

electrode reaction, and the transfer resistances are 195 Ω and 230 Ω after 100 cycles and 500 cycles, respectively [75], which are all larger than those of CHS@CG. The result shows that the addition of rGO nanosheets improves the electrical conductivity of the composites and greatly speeds up ion/electron transport in the process of lithiation/delithiation [76].

The Li$^+$ insertion/extraction processes of CHS@CG are schematically illustrated in Scheme 2. During the first discharge, an irreversible chemical reaction takes place in electrode material, and Li$_2$O, Co, and Li$_x$C

nanodispersed metallic particles are formed in the spherical shell and between the spherical shell and the carbon layer. In subsequent cycles, the electrode material shows good redox reversibility, and the nanodispersed metallic particles (Co) can effectively make extra Li$_2$O reversibly convert to Li$^+$, which can maintain a high capacity during the charge–discharge cycles [77, 78]. Furthermore, the carbon layer outside limits the volume change of the hollow nanospheres and ensures good cycling stability.

Table 1 Electrochemical performance comparison of the CHS@C and CHS@CG with the literature

Electrode material	Specific capacity (mAh·g^{-1})	Current density (mA·g^{-1})	Cycle number	References
CHS@C	645	200 (0.2C)	400	This work
CHS@CG	831	200 (0.2C)	400	This work
Co$_3$O$_4$@TiO$_2$ core-shell nanorods	803	200	100	[67]
Peapod-like Co$_3$O$_4$@CNT	700	100	100	[68]
Co$_3$O$_4$ hollow dodecahedra	780	100	100	[69]
Co$_3$O$_4$/multiwalled carbon nanotubes	813	100	100	[70]
Ni-Co/CoO/NC	218.7	500	100	[71]
Ni$_3$S$_2$/Co$_9$S$_8$/N–C	419.9	100	100	[72]
CoSnO$_3$-Co$_3$O$_4$ hollow nanospheres	569	1000	200	[73]
P-CoS	781	200	100	[74]
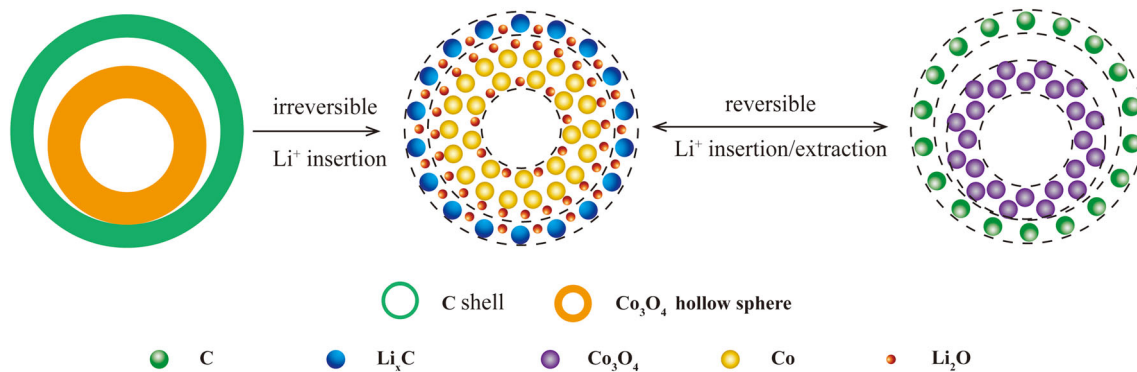
Scheme 2 Li$^+$ insertion/extraction mechanism for CHS@CG.

The as-prepared CHS-400 materials exhibit excellent Li-storage capacity, structure stability, and rate capability due to the good electrical conductivity and the synergistic effect of the interface among Co$_3$O$_4$, graphene, and pyrolytic carbon [50]. The synthesis method has the advantages of simple operation steps, strong repeatability, and versatility.

Conclusion

In conclusion, two carbon-wrapped Co$_3$O$_4$ hollow sphere structures were obtained from ZIF-12-PVP via molecular precursor pyrolysis in an air atmosphere. The main phase of the CHS@C and CHS@CG heat-treated at 400 °C was found Co$_3$O$_4$ and carbonized ZIF-12. Due to the large specific surface area, abundant active sites, shortened electron transport path, and sufficient cavities in the shell, the composite anode materials exhibit superior electrochemical performances. The reversible specific capacities reach up to 645 and 831 mAh·g^{-1} after 400 cycles at the rate of 0.2 C. In the constant charging and discharging process, the Coulombic efficiency reaches nearly 100%, exhibiting a good reversible cycle. The preparation method is simple, universal, and repeatable. This superior synthesis strategy will provide a new means of increasing the storage capacity of battery electrode materials and promising applications in the next-generation safer high-performance energy-storage systems.

Acknowledgements

Declaration

Competing interest The authors declare no competing financial interest.

Supplementary Information: The online version contains supplementary material available at http s://doi.org/10.1007/s10853-022-08047-1.

References

[1] Düehnen S, Betz J, Kolek M, Schmuch R, Winter M, Placke T (2020) Toward green battery cells: Perspective on materials and technologies. Small Methods 4(7):2070023

[2] Cresce AV, Xu K (2021) Aqueous lithium-ion batteries. Carbon Energy 3(5):721–751

[3] Galos J, Pattarakunnan K, Best AS, Kyratzis IL, Wang CH, Mouritz AP (2021) Energy storage structural composites with integrated lithium-ion batteries: A review. Adv Mater Technol 6:2001059

[4] Wu YP, Huang XK, Huang L, Chen JH (2020) Strategies for rational design of high-power lithium-ion batteries. Energy Environ Mater 4(1):19–45

[5] Lang XS, Wang XX, Liu Y, Cai KD, Li L, Zhang QG (2021) Cobalt-based metal organic framework (Co-MOFs)/graphene oxide composites as high-performance anode active materials for lithium-ion batteries. Int J Energ Res 45(3):4811–4820

[6] Wang JK, Wang HK, Li F, Xie SM, Xu GY, She YY, Leung MKH, Liu TX (2019) Oxidizing solid Co into hollow Co_3O_4 within electrospun (carbon) nanofibers towards enhanced lithium storage performance. J Mater Chem A 7:3024–3030

[7] Fang S, Bresser D, Passerini S (2019) Transition metal oxide anodes for electrochemical energy storage in lithium-and sodium-ion batteries. Adv Energy Mater 10(1):1902485

[8] Wang DL, Yu YC, He H, Wang J, Zhou WD, Abruna HD (2015) Template-free synthesis of hollow-structured Co_3O_4 nanoparticles as high-performance anodes for lithium-ion batteries. ACS Nano 9(2):1775–1781

[9] Kim J, Chung MK, Ka BH, Ku JH, Park S, Ryu J, Oh SM (2010) the role of metallic Fe and carbon matrix in Fe_2O_3/Fe/carbon nanocomposite for lithium-ion batteries. J Electrochem Soc 157(4):412–417

[10] Ke FS, Huang L, Zhang B, Wei GZ, Xue LJ, Li JT, Sun SG (2012) Nanoarchitectured Fe_3O_4 array electrode and its excellent lithium storage performance. Electrochim Acta 78:585–591

[11] Li T, Li XH, Wang ZX, Guo HJ, Hu QY, Peng WJ (2016) Robust synthesis of hierarchical mesoporous hybrid NiO-$MnCo_2O_4$ microspheres and their application in Lithium-ion batteries. Electrochim Acta 191:392–400

[12] Ko S, Lee JI, Yang HS, Park S, Jeong U (2012) Mesoporous CuO particles threaded with CNTs for high-performance lithium-ion battery anodes. Adv Mater 24(32):4451–4456

[13] Wang Q, Zhang DA, Wang Q, Sun J, Xing LL, Xue XY (2014) High electrochemical performances of alpha-MoO_3@MnO_2 core-shell nanorods as lithium-ion battery anodes. Electrochim Acta 146:411–418

[14] Poizot P, Laruelle S, Grugeon S, Dupont L, Tarascon JM (2000) Nano-sized transition-metaloxides as negative-electrode materials for lithium-ion batteries. Nature 407:496–499

[15] Pham TN, Bui VKH, Lee YC (2021) Recent advances in hierarchical anode designs of TiO_2-B nanostructures for lithium-ion batteries. Int J Energy Res 45(12):17532–17562

[16] Hu XR, Wei LS, Chen R, Wu QS, Li JF (2020) Reviews and prospectives of Co_3O_4-based nanomaterials for supercapacitor application. ChemistrySelect 5(17):5268–5288

[17] Yang YX, Chen X, Cao YL, Zhou WY, Sun H, Chai H (2020) Synthesis of homogeneous hollow Co_3O_4 microspheres for enhanced cycle life and electrochemical energy storage performance. ChemElectroChem 7(3):723–729

[18] Zhang CL, Lu BR, Cao FH, Yu ZL, Cong HP, Yu SH (2018) Hierarchically structured Co_3O_4@carbon porous fibers derived from electrospun ZIF-67/PAN nanofibers as anodes for lithium ion batteries. J Mater Chem A 6:12962–12968

[19] Kumar S, Srivastava R, Pak D, Chattopadhyay J (2021) Synthesis and energy applications of multi-shell micro/nanospheres. Int J Energy Res 45(10):14389–14413

[20] Aijaz A, Masa J, Rosler C, Xia W, Weide P, Botz AJR, Fischer RA, Schuhmann W, Muhler M (2016) Co@Co_3O_4 encapsulated in carbon nanotube-grafted nitrogen-doped carbon polyhedra as an advanced bifunctional oxygen electrode. Angew Chem Int Ed 55(12):4087–4091

[21] Wang CW, Tseng J, Peng SF, Hwu YK, Lin CK (2012) Functionalized polymer spheres via one-step photoinduced synthesis for antimicrobial activity and gene delivery. Nanotechnology 23(25):255103

[22] Mutuma BK, Matsoso B, Ranganathan K, Wamwangi D, Coville NJ (2016) Generation of open-ended, worm-like and graphene-like structures from layered spherical carbon materials. RCS Adv 6:20399–20408

[23] Li M, Zhang JY, Gao H, Li F, Lindquist SE, Wu NQ, Wang RM (2016) Microsized BiOCl square nanosheets as ultraviolet photodetectors and photocatalysts. ACS Appl Mater Interfaces 8(10):6662–6668

[24] Luo JM, Tao XY, Zhang J, Xia Y, Huang H, Zhang LY, Gan YP, Liang C, Zhang WK (2016) Sn^{4+} ion decorated highly conductive Ti_3C_2 MXene: promising lithium-ion anodes

with enhanced volumetric capacity and cyclic performance. ACS Nano 10(2):2491–2499

[25] Yang C, Yao Y, Lian YB, Chen YJ, Shah R, Zhao XH, Chen MZ, Peng Y, Deng Z (2019) A double-buffering strategy to boost the lithium storage of botryoid MnO_x/C anodes. Small 15(16):1900015

[26] Buğday N, Altin E, Altin S, Yaşar S (2022) High-performance electrodes for Li-ion cell: heteroatom-doped porous carbon/CoS structure and investigation of their structural and electrochemical properties. Int J Energy Res 46(13):18379–18393

[27] Zhang ZC, Chen YF, Xu XB, Zhang JC, Xiang GL, He W, Wang X (2014) Well-defined metal-organic framework hollow nanocages. Angew Chem Int Ed 126(2):439–433

[28] Ameloot R, Vermoortele F, Vanhove W, Roeffaers MBJ, Sels BF, De Vos DE (2011) Interfacial synthesis of hollow metal-organic framework capsules demonstrating selective permeability. Nat Chem 3(5):382–387

[29] Cheng EB, Huang SS, Chen YD, Huang RT, Wang Q, Hu ZJ, Jiang Y, Li Z, Zhao B, Chen ZW (2019) Porous ZnO/Co_3O_4/N-doped carbon nanocages synthesized via pyrolysis of complex metal-organic framework (MOF) hybrids as an advanced lithium-ion battery anode. Acta Crystallogr C 75(7):969–978

[30] Li JH, Li FY, Liao JY, Li H, Dang D, Liu QB, Peng HJ (2020) Scalable construction of hollow multishell Co_3O_4 with mitigated interface reconstruction for efficient lithium storage. Adv Mater Interfaces 7(14):2000667

[31] Yan CS, Chen G, Zhou X, Sun JX, Lv CD (2016) Template-based engineering of carbon-doped Co_3O_4 hollow nanofibers as anode materials for lithium-ion batteries. Adv Funct Mater 26(9):1428–1436

[32] Chen YM, Yu L, Lou XW (2016) Hierarchical tubular structures composed of Co_3O_4 hollow nanoparticles and carbon nanotubes for lithium storage. Angew Chem Int Ed 55(20):5990–5993

[33] Zhang X, Dong P, Song MK (2019) Metal-organic frameworks for high-energy lithium batteries with enhanced safety: recent Progress and future perspectives. Batter Supercaps 2(7):591–626

[34] Kaneti YV, Tang J, Salunkhe RR et al (2017) Nanoarchitectured design of porous materials and nanocomposites from metalorganic frameworks. Adv Mater 29(12):1604898

[35] Wu YZ, Meng JS, Li Q, Niu CJ, Wang XP, Yang W, Li W, Mai LQ (2017) Interface-modulated fabrication of hierarchical yolk-shell Co_3O_4/C dodecahedrons as stable anodes for lithium and sodium storage. Nano Res 10:2364–2376

[36] Wang L, Wan JW, Wang JY, Wang D (2021) Small structures bring big things: performance control of hollow multishelled structures. Small Struct 2(1):2000041

[37] Mao D, Wan JW, Wang JY, Wang D (2019) Sequential templating approach: a groundbreaking strategy to create hollow multishelled structures. Adv Mater 31(38):1970274

[38] Wang JY, Wan JW, Yang NL, Li Q, Wang D (2020) Hollow multishell structures exercise temporal-spatial ordering and dynamic smart behaviour. Nat Rev Chem 4:159–168

[39] Wang JY, Wan JW, Wang D (2019) Hollow multishelled structures for promising applications: understanding the structure-performance correlation. Acc Chem Res 52(8):2169–2178

[40] Zhu MY, Tang JJ, Wei WJ, Li SJ (2020) Recent progress in the syntheses and applications of multishelled hollow nanostructures. Mater Chem Front 4:1105–1149

[41] Zhao JL, Yang M, Yang NL, Wang JY, Wang D (2020) Hollow micro-/nanostructure reviving lithium-sulfur batteries. Chem Res Chin Univ 36:313–319

[42] Wang ZM, Yang NL, Wang D (2020) When hollow multishelled structures (HoMSs) meet metal-organic frameworks (MOFs). Chem Sci 11(21):5359–5368

[43] Zhang ZF, Su XR, Zhu YY, Fang ZB, Luo XJ, Chen ZH (2020) Polypyrrole encapsulation-protected porous multishelled Co_3O_4 hollow microspheres for advanced all-solid-state asymmetric supercapacitors with boosted reaction kinetics and stability. Nanotechnology 31(25):255403

[44] Choi WH, Moon BC, Park DG, Choi JW, Kim KH, Shin JS, Kim MG, Choi KM, Kang JK (2020) Autogenous production and stabilization of highly loaded sub-nanometric particles within multishell hollow metal-organic frameworks and their utilization for high performance in LiO_2 batteries. Adv Sci 7(9):2000283

[45] Ren H, Yu RB (2019) Hollow multi-shelled structures for energy conversion and storage applications. Inorg Chem Front 6:2239–2259

[46] Buğday N, Ates MN, Duygulu O, Deng WT, Ji XB, Altin S, Yaşar S (2022) ZIF-12-derived N-doped Fe/Co/S/@C nanoparticles as high-performance composite anode electrode materials for lithium-ion batteries. J Alloys Compd 928:67037

[47] Yin LH (2013) Study on the anode materials of Mn-Co_3O_4 for lithium ion secondary batteries. Asian J Chem 25(2):1155–1156

[48] Du HM, Jiao LF, Wang QH, Wang YJ, Yuan HT (2013) Facile carbonaceous microsphere templated synthesis of Co_3O_4 hollow spheres and their electrochemical performance in supercapacitors. Nano Res 6:87–98

[49] Zhang DH, Zou WB (2013) Decorating reduced graphene oxide with Co_3O_4 hollow spheres and their application in supercapacitor materials. Curr Appl Phys 13(8):1796–1800

[50] Li ZS, He MM, Bo B, Wei HJ, Liu YY, Wen H, Liu YS, Zhang K, Zhang PK, Li BJ (2021) Bi_2S_3 nanorods hosted on

rGO sheets from pyrolysis of molecular precursors for efficient Li-Ion storage. Energy Environ Mater 4(4):577–585

[51] Liu YY, Sun K, Jiang JC, Zhou WS, Shang Y, Du CX, Li BJ (2021) Metallurgical pyrolysis toward Co@Nitrogen-doped carbon composite for lithium storage. Green Energy Environ 6(1):91–101

[52] He M, Yao JF, Liu Q, Zhong ZX, Wang HT (2013) Toluene-assisted synthesis of RHO-Type zeolitic imidazolate frameworks: synthesis and formation mechanism of ZIF-11 and ZIF-12. Dalton T 42(47):16608–16613

[53] Mei WM, Huang J, Zhu LP, Ye ZZ, Mai YJ, Tu JP (2012) Synthesis of porous rhombus-shaped Co_3O_4 nanorod arrays grown directly on a nickel substrate with high electrochemical performance. J Mater Chem 22(18):9315–9321

[54] Wang JY, Yang NL, Tang HJ, Dong ZH, Jin Q, Yang M, Kisailus D, Zhao HJ, Tang ZY, Wang D (2013) Accurate control of multishelled Co_3O_4 hollow microspheres as high-performance anode materials in lithium-ion batteries. Angew Chem Int Ed 52(25):6417–6420

[55] Xing CC, Liu YY, Su YH, Chen YH, Hao S, Wu XL, Wang XY, Cao HQ, Li BJ (2016) Structural evolution of Co-based metal organic frameworks in pyrolysis for synthesis of core-shells on nanosheets: $Co@CoO_x@Carbon-rGO$ composites for enhanced hydrogen generation activity. ACS Appl Mater Interfaces 8(24):15430–15438

[56] Huang GY, Xu SM, Lu SS, Li LY, Sun HY (2014) Micro-/nanostructured Co_3O_4 anode with enhanced rate capability for lithium-ion batteries. ACS Appl Mater Interfaces 6(10):7236–7243

[57] Madej E, Klink S, Schuhmann W, Ventosa E, Mantia FL (2015) Effect of the specific surface area on thermodynamic and kinetic properties of nanoparticle anatase TiO_2 in lithium-ion batteries. J Power Sources 297:140–148

[58] Zhang SS (2020) Challenges and strategies for fast charge of Li-ion batteries. ChemElectroChem 7(17):3569–3577

[59] Zhai XM, Yang W, Li MY, Lu GQ, Liu JP, Zhang XL (2013) Noncovalent hybrid of $CoMn_2O_4$ spinel nanocrystals and poly (diallyldimethylammonium chloride) functionalized carbon nanotubes as efficient electrocatalysts for oxygen reduction reaction. Carbon 65:277–286

[60] Liu HC, Yen SK (2007) Characterization of electrolytic Co_3O_4 thin films as anodes for lithium ion batteries. J Power Sources 166(2):478–484

[61] Wang YF, Li XS, He MM, Du H, Wu XL, Hao JH, Li BJ (2019) Core-shells on nanosheets: Fe_3O_4@carbon-reduced graphene oxide composites for lithium-ion storage. J Solid State Electr 23:237–244

[62] Zhao LZ, Wu HH, Yang CH, Zhang QB, Zhong GM, Zheng ZM, Chen HX, Wang JM, He K, Wang BL, Zhu T, Zeng XC, Liu ML, Wang MS (2018) Mechanistic origin of the high performance of Yolk@Shell Bi_2S_3@N-doped carbon nanowire electrodes. ACS Nano 12(12):12597–12611

[63] Banerjee R, Phan A, Wang B, Knobler C, Furukawa H, O'Keeffe M, Yaghi OM (2008) High-throughput synthesis of zeolitic imidazolate frameworks and application to CO_2 capture. Science 319(5865):939–943

[64] Ge XH, Yuan BH, Xu S, Xu P, Shi YP, Liu YY, Li ZS, Sun Q, Guo J, Liang EJ, Li BJ (2020) Anodic lithium ion battery material with negative thermal expansion. Ceram Int 46(11):19127–19134

[65] Li L, Zhang ZC, Ren SJ, Zhang BK, Yang SH, Cao BQ (2017) Construction of hollow Co_3O_4 cubes as a high-performance anode for lithium ion batteries. New J Chem 41(16):7960–7965

[66] Xu DY, Mu CP, Xiang JY, Wen FS, Su C, Hao CX, Hu WT, Tang YF, Liu ZY (2016) Carbon-encapsulated Co_3O_4@-CoO@Co nanocomposites for multifunctional applications in enhanced long-life lithium storage, supercapacitor and oxygen evolution reaction. Electrochim Acta 220:322–330

[67] Geng HB, Ang HX, Ding XG, Tan HT, Guo GL, Qu GL, Yang YG, Zheng JW, Yan QY, Gu HW (2016) Metal coordination polymer derived mesoporous Co_3O_4 nanorods with uniform TiO_2 coating as advanced anodes for lithium ion batteries. Nanoscale 8:2967

[68] Gu D, Li W, Wang F, Bongard H, Spliethoff B, Schmidt W, Weidenthaler C, Xia YY, Zhao DY, Schüth F (2015) Controllable synthesis of mesoporous peapod-like Co_3O_4@-carbon nanotube arrays for high-performance lithium-ion batteries. Angew Chem Int Ed 54(24):7060–7064

[69] Wu RB, Qian XK, Rui XH, Liu H, Yadian B, Zhou K, Wei J, Yan QY, Feng XQ, Long Y, Wang LY, Huang YZ (2014) Zeolitic imidazolate framework 67-derived high symmetric porous Co_3O_4 hollow dodecahedra with highly enhanced lithium storage capability. Small 10:1932

[70] Huang G, Zhang F, Du X, Qin Y, Yin D, Wang L (2015) Metal organic frameworks route to in situ insertion of multiwalled carbon nanotubes in Co_3O_4 polyhedra as anode materials for lithium-ion batteries. ACS Nano 9(2):1592–1599

[71] Kaneti YV, Zhang J, He Y, Wang Z, Tanaka S, Hossain MSA, Pan Z, Xiang B, Yang Q, Yamauchi Y (2017) Fabrication of an MOF-derived heteroatom-doped Co/CoO/carbon hybrid with superior sodium storage performance for sodium-ion batteries. J Mater Chem A 5:15356–15366

[72] Liu X, Zou F, Liu K, Qiang Z, Taubert CJ, Ustriyana P, Vogt BD, Zhu Y (2017) A binary metal organic framework derived hierarchical hollow Ni_3S_2/Co_9S_8/N-doped carbon composite with superior sodium storage performance. J Mater Chem A 5:11781–11787

[73] Park G, Kang Y (2018) Design and synthesis of spherical multicomponent aggregates composed of core-shell, yolk-shell, and hollow nanospheres and their lithium-ion storage performances. Small 14(13):1703957

[74] Wang B, Cheng YF, Su H, Cheng M, Li Y, Geng HB, Dai ZF (2020) Boosting transport kinetics of cobalt sulfides yolk-shell spheres by anion doping for advanced lithium and sodium storage. Chemsuschem 13(16):4078–4085

[75] Reddy MV, Prithvi G, Loh KP, Chowdari BVR (2014) Li storage and impedance spectroscopy studies on Co_3O_4, CoO, and CoN for Li-Ion batteries. ACS Appl Mater Interfaces 6(1):680–690

[76] Dou YH, Xu JT, Ruan BY, Liu QN, Pan YD, Sun ZQ, Dou SX (2016) Atomic layer-by-Layer Co_3O_4/graphene composite for high performance lithium-ion batteries. Adv Energy Mater 6(8):1501835

[77] Wang Q, Yu BW, Li X, Xing LL, Xue XY (2016) Core-shell Co_3O_4/$ZnCo_2O_4$ coconut-like hollow spheres with extremely high performance as anode materials for lithium-ion batteries. J Mater Chem A 4:425–433

[78] Zhang QB, Chen HX, Han X, Cai JJ, Yang Y, Liu ML, Zhang KL (2016) Graphene-encapsulated nanosheet-assembled zinc-nickel-cobalt oxide microspheres for enhanced lithium storage. Chemsuschem 9(2):186–196